Nat. Hazards Earth Syst. Sci., 17, 657–670, 2017
www.nat-hazards-earth-syst-sci.net/17/657/2017/
doi:10.5194/nhess-17-657-2017

Natural Hazards and Earth System Sciences
Open Access
EGU

Analysis of the Tangjiaxi landslide-generated waves in the Zhexi Reservoir, China, by a granular flow coupling model

Bolin Huang[1,2], Yueping Yin[3], Shichang Wang[2], Jianmin Tan[2], and Guangning Liu[2]

[1]China Three Gorges University, Hubei Key laboratory of Disaster Prevention and Mitigation, Yichang, China
[2]Wuhan Center of China Geological Survey, Wuhan, China
[3]China Institute for Geo-Environmental Monitoring, Beijing, China

Correspondence to: Bolin Huang (bolinhuang@aliyun.com)

Received: 12 October 2016 – Discussion started: 4 January 2017
Revised: 6 April 2017 – Accepted: 8 April 2017 – Published: 11 May 2017

Abstract. A rocky granular flow is commonly formed after the failure of rocky bank slopes. An impulse wave disaster may also be initiated if the rocky granular flow rushes into a river with a high velocity. Currently, the granular mass–water body coupling study is an important trend in the field of landslide-induced impulse waves. In this paper, a full coupling numerical model for landslide-induced impulse waves is developed based on a non-coherent granular flow equation, i.e., the Mih equation. In this model, the Mih equation for continuous non-coherent granular flow controls movements of sliding mass, the two-phase flow equation regulates the interaction between sliding mass and water, and the renormalization group (RNG) turbulence model governs the movement of the water body. The proposed model is validated and applied for the 2014 Tangjiaxi landslide of the Zhexi Reservoir located in Hunan Province, China, to analyze the characteristics of both landslide motion and its following impulse waves. On 16 July 2014, a rocky debris flow was formed after the failure of the Tangjiaxi landslide, damming the Tangjiaxi stream and causing an impulse wave disaster with three dead and nine missing bodies. Based on the full coupling numerical analysis, the granular flow impacts the water with a maximum velocity of about 22.5 m s^{-1}. Moreover, the propagation velocity of the generated waves reaches up to 12 m s^{-1}. The maximum calculated run-up of 21.8 m is close enough to the real value of 22.7 m. The predicted landslide final deposit and wave run-up heights are in a good agreement with the field survey data. These facts verify the ability of the proposed model for simulating the real impulse wave generated by rocky granular flow events.

1 Introduction

Impulse waves are usually generated in reservoirs, rivers, lakes, and seas as rock/soil masses impact water, resulting in huge economic losses and casualties (Wang et al., 1986; Fritz 2001; Scheffers and Kelletat, 2003; Alvarez-Cedrón et al., 2009; Silvia et al., 2011; Huang et al., 2012). This fact urges people to pay attention to landslide-induced impulse waves, which is an interdisciplinary study related to rock/soil mechanics and fluid mechanics. A large number of studies have been done on landslide-induced impulse waves, including analytical, physical, and numerical methods. The analytical solutions are derived from extensive sources, such as experimental and empirical formulae, where their application scope is limited to their sources (Kamphuis et al., 1970; Ataie-Ashtiani et al., 2008; Wieland et al., 1999; Ursell et al., 1960; Fritz et al., 2002; Huber and Hager, 1997; Heller, 2007; Yin and Wang, 2008). Due to the considered simplifications for analytical solutions, it is hard to have an overall grasp of the landslide-induced impulse wave disaster (Heller et al., 2009). The scaled physical experiment method can well reproduce or preview the dynamic process of landslide-induced impulse waves (Ball, 1970; Davidson and Whalin, 1974; Muller and Schurter, 1993). However, it requires a large amount of data, time, and money and occupies a large amount of space (Huang et al., 2014). However, the numerical analysis method can help us have a relatively comprehensive analysis of the landslide-induced impulse wave disaster; it has the advantages of being precise, economic, and reasonable, as well as having highly visible results (Heller et al., 2009). Therefore, the numerical analysis method is an effi-

cient tool in the study of landslide-induced impulse waves (Yavari-Ramshe and Ataie-Ashtiani, 2016).

Regarding the granular mass–water body coupling system, three major numerical simulation methods have been recently applied, such as (a) single model, (b) simplified model, and (c) full coupling model (Yavari-Ramshe and Ataie-Ashtiani, 2016). Each model may apply a mesh-based (e.g., finite difference method, finite element method, FEM; finite volume method, boundary element method) or a particle-based (smoothed particle hydrodynamic, material particle method, etc.) method (Yavari-Ramshe and Ataie-Ashtiani, 2016) for numerical discretization of its model equations. In the single simulation method for a landslide-induced impulse wave, the phase of landslide movement and granular mass–water body interaction is regarded as the formation of the initial impulse wave, and generally the motion of the sliding mass is considered to the motion of a rigid block. Therefore, various kinematic formulas, such as Newton's laws of motion, are applied to calculate the motion of the sliding mass (Heller, 2009; Huang et al., 2012, 2016). Then, various empirical or experimental formulas of landslide-induced impulse waves are adopted to calculate the characteristics of the initial impulse wave caused by the landslide (Walder et al., 2003; Tappin et al., 2008; Watts et al., 2003; Ataie-Ashtiani and Malek Mohammadi, 2007). With the initial impulse wave as the initial input or boundary condition, the numerical simulation singularly aims at calculating the spread and run-up of impulse waves. Some examples of these models are TUNAMI (Fumihiko et al., 2006), MOST (Titov and Gonzalez, 1997), FUNWAVE (Joseph et al., 2003; Tappin et al., 2008), and CLAWPACK (Randall, 2006). Their accuracy and application scope largely depend on the source models for the initial impulse wave. Many scholars (Watts et al., 2003; Ataie-Ashtiani and Malek-Mohammadi, 2008; Di Risio et al., 2011; Yin et al., 2015c) have studied initial impulse wave models in a different range of application and introduced a large number of source models.

The simplified simulation for the landslide-induced impulse wave aims to simplify landslide motion in calculation. Some landslides are simplified as rigid bodies whose motion is mainly described with Newton's laws of motion such as gravity, friction, and coupled water resistance (Das et al., 2009; Basu et al., 2009; Huang et al., 2013). For example, Yin et al. (2015a) simulated the motion of the Qianjiangping landslide as a rigid rotator and calculated the impulse waves. Harbitz et al. (2014) simulated a rockslide with the volume of 5×10^7 m^3 at Åkerneset fjord, western Norway, as a rigid sliding block. Such simplified methods can reveal the rules of how various dynamic models of a rigid body affect impulse waves (Yin et al., 2015b). For some flow-like slides or debris flow, simple fluids or grains are used to simulate large deformation in the process of the motion of landslide. For instance, Ren et al. (2006) simulated the motion of Xintan landslide by regarding it as some large grains which comply with Newton's laws of motion and the law of conservation of energy. Gabl et al. (2015) used fluid to simulate landslides occurring at hillsides and the following impulse waves. Abadie et al. (2010) adopted the multi-phase flow model to simulate landslide-induced impulse waves, as a Newtonian fluid simulating the landslide. In these studies, simple fluids or grains are used for simplified simulation, and thus the effects of landslide deformation on landslide-induced impulse waves could be taken into consideration at least partly in calculation.

The full coupling model for landslide-induced impulse waves is a currently emerging method, which has been receiving considerable attention recently. The full coupling model can have a relatively accurate description of the motion of sliding mass, interaction with water, and consequent impulse waves. Simplified models have obvious difficulties in achieving an accurate description of the landslide motion. Accordingly, numerical models which consider the rheological behavior of the sliding mass in their calculations have been recently applied more often. The most applied continuous rheological models so far include the Coulomb model, Herschel–Bulkley model, Bagnold model, and Bingham model (Shakeri Majd and Sanders, 2014; Cremonesi et al., 2011; Yavari-Ramshe and Ataie-Ashtiani, 2016; Xing et al., 2016). Those that describe avalanche, landslide, or debris flow motions in discontinuous medium models are mainly the FEM–discrete element method model (FEM–DEM; Morris et al., 2006; Munjiza, 2004; Li et al., 2015) and DEM model (Smilauer et al., 2010; Brennen, 2005; Utili et al., 2014). For generation, propagation, and run-up of impulse waves, technologies that can finely depict large free-surface deformations, such as VOF (volume of fluid) or non-hydrostatic models (Yavari-Ramshe and Ataie-Ashtiani, 2016), are adopted. Crosta et al. (2013) used an arbitrary Lagrangian–Eulerian–FEM (ALE–FEM) approach for a 2-D–3-D simulation of landslide and impulse wave. Glimsdal et al. (2013) developed a model for submarine landslide and tsunami, where the landslide motion was simulated as a deformable viscoplastic Bingham fluid. Zhao et al. (2015) used a 3-D DEM–computational fluid dynamics (DEM–CFD) coupling method to simulate the motion of the Vajont landslide and the resulting impulse waves. By combining a landslide dynamic model and a tsunami model, Sassa (2016) presented an integrated numerical model simulating the complete evolution of a landslide-induced tsunami. This model was applied to the 1792 Unzen–Mayuyama mega-slide and tsunami disaster analysis.

In this paper, a full coupling model is developed for landslide-induced impulse waves based on a non-coherent granular flow equation. The continuous granular flow model of Mih (1999) is applied to simulate the motion process of the rocky granular flow after rockslide. Then, a two-phase flow model is adopted for granular mass–water interaction coupled calculation. Taking the Tangjiaxi rockslide and the resulting impulse wave as a case, a numerical analysis for the whole process is done to study the motion of the granu-

lar flow, its accumulation process and consequent formation, propagation, and run-up of impulse waves. Meanwhile, the validity of the full coupling model for landslide-induced impulse is checked.

2 Theory and methodology

Rockslides can be characterized by a rapid evolution, up to a possible transition into a rock avalanche, which can be associated with an almost instantaneous collapse and spreading (Utili et al., 2014). The failure of a rocky slope is commonly followed by a high-concentration and non-coherent rocky granular motion. A large number of non-coherent coarse solid grains as well as relatively few fine grains are densely distributed in the granular flows. They flow, deposit, or erode along their motion routes, which generally span long distances (Crosta et al., 2001). Such flowing characteristics of motion can be described through both the continuous rheological model and the discontinuous model. The discontinuous model for particle flow simulation has a natural similarity. For the discontinuous method, grains are generally simplified to be a sphere. These grains can interact with each other through well-defined microscopic contact models (Hertz, 1882; Zhang and Whiten, 1996; Johnson, 1985) and with the fluid (e.g., water or air) by empirical correlations of fluid and solid interaction models. However, the discontinuous method means a large challenge for individual researchers. That is because even for a small rockslide, the simulation will require numerous cells and huge computational resources, which is hard to process with personal computers (Utili and Crosta, 2011), whereas the model based on continuous granular flow is free from this problem.

High-concentration granular flow was studied by several researchers such as Bagnold (1954), Savage (1978), Hanes and Inman (1985), Wang and Campbell (1992), Iverson (1997), and Mih (1999). Some rheological models such as Coulomb and Voellmy consider no viscosity or shear rate in their rheological formulations (Iverson, 1997). In this study, the present continuous granular flow model is built using viscous fluid.

2.1 Governing equations of granular flow

Landslide rheology describes landslide motions with shear stress (τ) or shear rate (Pudasaini, 2011). Shear stress of granular flow is generally far larger than the cohesive shear stress of fluids that carry a small amount of grains. Shear stress in high-concentration non-cohesive granular flow (τ_g) consists of (1) impact among solid particles (τ_i), (2) additional viscous shear stress due to the presence of solid particles (τ_v), and (3) shear stress in the fluid (τ_f) (Mih, 1999). It becomes negligible in solid–gas flow when the dynamic viscosity of the gas is small. At high concentrations the principal contribution to the shear stress arises from impact forces (i.e., collision) among grains. Secondly, in general, a smaller contribution arises from the distributed solid affecting the fluid. Bagnold (1954) performed shear cell experiments with different approaches and showed that an equation for cohesionless materials describes the relationship between bulk intergranular normal and shear stresses even in collision-dominated flows.

Extensive work, beginning with the 1954 work of Bagnold (1954) has been summarized and further extended to a larger range of experimental conditions by Mih (1999). He described the shear stress of a granular flow as follows:

$$\tau_g = \tau_v + \tau_i = 7.8\mu \frac{\lambda^2}{1+\lambda}\frac{du}{dy} + \rho_S \frac{0.015}{1+0.5\rho/\rho_g}\frac{1+e}{(1-e)^{0.5}}(\lambda D\frac{du}{dy})^2. \quad (1)$$

Here μ and ρ are the continuous fluid viscosity and fluid density between grains (e.g., air or water), ρ_g is the granular density, e is the coefficient of restitution associated with grain impacts, D is the grain diameter, and d is a function of the maximum solid volume fraction. Physically, $\lambda = d/S$, where S is defined as the average distance between grain centers. u is the mean velocity of the granular flow, y is the distance along the direction vertical to the moving direction, and du/dy is the mean velocity gradient of the granular mixture.

The equation contains fluid viscous and impact coefficients. The fluid viscous coefficient is a constant. The impact coefficient has been correlated to the properties of the solid and fluid. The equation agrees reasonably well with several sets of experiments by different investigators which cover a wide range of granular flows (Mih, 1999).

2.2 Granular flow–fluid interaction

The granular flow is treated as incompressible fluid when applied with the shear stress equation of Mih (1999). The coupling model of granular flow and water adopts a two-phase model with two incompressible fluids having different densities. Supposing the water has density ρ_1, the granular flow has density ρ_2. The volume fraction of the water making up a mixture is denoted by f, and the volume fractions of the grains are denoted by $1-f$. The momentum balance for the continuous phase of water is

$$\frac{\partial u_1}{\partial t} + u_1 \cdot \nabla u_1 = -\frac{1}{\rho_1}\nabla P + F + \frac{K}{f\rho_1}u_r, \quad (2)$$

while for the dispersed phase or the granular it is

$$\frac{\partial u_2}{\partial t} + u_2 \cdot \nabla u_2 = -\frac{1}{\rho_2}\nabla P + F - \frac{K}{(1-f)\rho_2}u_r, \quad (3)$$

where u_1 and u_2 represent the velocities of the continuous and dispersed phases, respectively; F is the body force; P is the pressure; K is a drag coefficient that relates to the interaction of the two phases; and u_r is the relative velocity

difference between the dispersed and continuous phases:

$$u_r = u_2 - u_1. \tag{4}$$

The volume-weighted average velocity $\overline{u}$ of a mixture is Eq. (5).

$$\overline{u} = f u_1 + (1 - f) u_2 \tag{5}$$

The volume-weighted average velocity momentum conservation equation is Eq. (6).

$$\nabla \cdot \overline{u} = 0 \tag{6}$$

The drag per unit volume (K) is calculated by Eq. (7).

$$K = \frac{1}{2} A_2 \rho_1 \left(C_D U + 12 \frac{\mu_1}{\rho_1 R_2} \right), \tag{7}$$

where A_2 is the cross-sectional area per unit volume of the dispersed phase, ρ_1 and μ_1 are the water density and dynamic viscosity, and C_D is the user-specified drag coefficient. It is a dimensionless quantity which is 0.5 for spheres.

R_2 is the average particle size of the granular.

2.3 Governing equations of fluid flow

The renormalization group (RNG) k-ε model is used to calculate the fluid motion when the granular flow enters the water. The RNG model applies statistical methods to the derivation of the average equations for turbulence quantities, such as turbulent kinetic energy and its dissipation rate. The RNG model uses equations similar to the ones for the k-ε model. However, equation constants are derived explicitly in the RNG model, and it takes turbulent vortex into account. Generally, the RNG model has a wider applicability than the standard k-ε model. The transport equation for K_T includes the convection and diffusion of the turbulent kinetic energy, the production of turbulent kinetic energy due to shearing and buoyancy effects, diffusion, and dissipation due to viscous losses within the turbulent eddies (Yakhot and Orszag, 1986; Yakhot and Smith, 1992). The transport equation for K_T is

$$\frac{\partial k_T}{\partial t} + \frac{1}{V_F}\left\{ u A_x \frac{\partial k_T}{\partial x} + v A_y \frac{\partial k_T}{\partial y} + w A_z \frac{\partial k_T}{\partial z} \right\} = P_T + G_T + \mathrm{Diff}_{k_T} - \varepsilon_T. \tag{8}$$

An additional transport equation is solved for the turbulent dissipation, ε_T:

$$\frac{\partial \varepsilon_T}{\partial t} + \frac{1}{V_F}\left\{ u A_x \frac{\partial k_T}{\partial x} + v A_y R \frac{\partial k_T}{\partial y} + w A_z \frac{\partial k_T}{\partial z} \right\} = \frac{\mathrm{CDIS1} \cdot \varepsilon_T}{k_T}(P_T + \mathrm{CDIS3} \cdot G_T) + \mathrm{Diff}_\varepsilon - \mathrm{CDIS2} \frac{\varepsilon_T^2}{k_T}. \tag{9}$$

In the RNG turbulence transport models, the kinematic turbulent viscosity V_T is computed from

$$v_T = \mathrm{CNU} \frac{k_T^2}{\varepsilon_T}.$$

The diffusion of dissipation, $\mathrm{Diff}_\varepsilon$, is

$$\mathrm{Diff}_\varepsilon = \frac{1}{V_F}\left\{ \frac{\partial}{\partial x}(v_\varepsilon A_x \frac{\partial \varepsilon_T}{\partial x}) + R \frac{\partial}{\partial y}(v_\varepsilon A_y R \frac{\partial \varepsilon_T}{\partial y}) + \frac{\partial}{\partial z}(v_\varepsilon A_z \frac{\partial \varepsilon_T}{\partial z}) + \xi \frac{v_\varepsilon A_x \varepsilon_T}{x} \right\}, \tag{10}$$

where k_T is the turbulent kinetic energy, V_F is the fractional volume open to flow, A_x is the fractional area open to flow in the x direction, and A_y and A_z are similar area fractions for the flow in the y and z directions, respectively. P_T is the turbulent kinetic energy production term, G_T is the buoyancy production term, and ε_T is the turbulence dissipation term. In the RNG model, CDIS1, CDIS3, and CNU are dimensionless user-adjustable parameters that have 1.42, 0.2, and 0.085 defaults. CDIS2 is computed from the turbulent kinetic energy (K_T) and turbulent production (P_T) terms (Yakhot and Orszag, 1986; Yakhot and Smith, 1992).

In particular, the RNG model is known to describe low-intensity turbulence flows and flows having strong shear regions more accurately. The RNG model selected has already been successfully used to simulate impulse waves generated by landslides (Serrano-Pacheco et al., 2009; Basu et al., 2009; Das et al., 2009; Choi et al., 2007).

3 Case study

A full coupling numerical analysis model for landslide-induced impulse waves is built based on coupled control equations. The model can stimulate the landslide motion of non-coherent granular flow and the generation, propagation, and run-up process of impulse waves. The Tangjiaxi landslide event in the Zhexi Reservoir, Hunan, China, is simulated as an example to analyze the whole process of the landslide motion and the impulse wave.

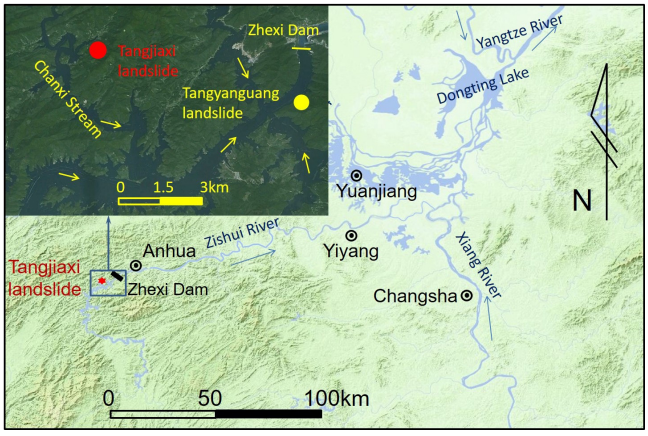

Figure 1. The location of the Tangjiaxi landslide in the Zhexi Reservoir, Hunan Province, China.

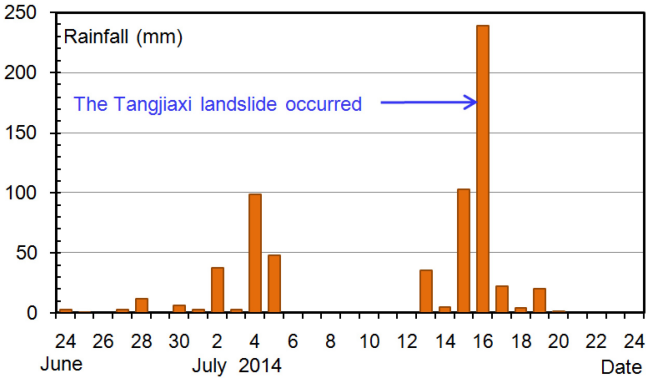

Figure 2. Precipitation data monitored in the village of Sifang, 3.6 km from the landslide.

Figure 3. Photo of first slide, taken by a local villager on 16 July, 07:00 LT.

3.1 Overview of the Tangjiaxi landslide and impulse wave

At 07:00 local time (LT) on 16 July, the Tangjiaxi landslide occurred on the left bank of the Tangjiaxi stream, a tributary of the Zhexi Reservoir. The impulse wave induced by the Tangjiaxi landslide destroyed the nearby residential area. The landslide is 700 m away from the mainstream of the Chanxi stream (tributary of Zi River) and 10.6 and 11.2 km away from the Tangyanguang landslide site and Zhexi Dam along the watercourse, respectively (Fig. 1). The Zhexi Dam is located in the midstream of Zi River in Anhua County, Yiyang City, Hunan Province, China, and 15 km away from the seat of Anhua County. The Zhexi hydroelectric station, which began to impound in February 1961, is a large hydroelectric station. The Tangyanguang landslide occurred on 6 March 1961. It is the first impulse wave disaster generated by landslide since the founding of the People's Republic of China. The huge wave generated by the Tangyanguang landslide overtopped Zhexi Dam and killed 64 individuals (Du, 1988). The impulse wave disaster generated by the landslide happened again in this reservoir, which drew more attention.

The landform of the Tangjiaxi stream valley belongs to the type of medium gorge. The elevation of the highest mountain in this valley is 650 m, while the bottom elevation is 140–170 m generally. The overall flow direction of the Tangjiaxi stream is 245°, with a large gradient about 1 km long. When water level elevation is 169.5 m, the stream is 2–100 m wide and 2–30 m deep. The original slope at valley bottom was about 25–30°, and that at altitude above 200 m was 35–45°. Generally, eluvial and diluvial deposits 2–5 m thick were developed in the slope of the valley, with lush vegetation cover.

The rain continued for almost half a month from late June to early July in 2014. The daily rainfall was 98.5 mm around 4 July. The Zhexi Reservoir was hit by a rainstorm on 13 July again. The rainfall reached 102.5 mm on 15 July and, more seriously, 239 mm on 16 July (Fig. 2). Rainfall increased the weight of sliding mass, formed greater underground water dynamic pressure, and decreased anti-sliding strength (Thomas, 2003; Wang et al., 2004). Persistent rainfalls and heavy rainstorm directly triggered the failure of the landslide.

According to the description of many local survivors, the first slide occurred around 07:00 LT on 16 July. Figure 3 shows the scene of the first slide. Starting from the toe of the slope, the first slide was a shallow soil slide which destroyed one of the three houses on the sliding mass. There was a short quiet period after the first slide. At about 10:20 LT, rock blocks rolled down from the top of the slope and the global slide started. As soon as the landslide mass started to run out, rocks broke, crashed and rumbled down to the slope foot, and

Figure 4. The scene of the Tangjiaxi landslide, taken on 23 July 2014, when the water level was 167 m a.s.l. The river was full of wood and debris, which were the destroyed building materials.

houses were buried quickly. The mass impacted the Tangjiaxi stream at a high speed and induced huge waves, and the still-water level was 169.5 m above sea level (a.s.l.).

As shown in Fig. 4, the morphology of the landslide scar was triangular in shape. The crown elevation of the landslide was about 315 m, and the elevation of the outlet was about 155 m. The height difference was 160 m. At 26 m above the water surface, the landslide was 95 m wide, and, at 56 m above the water surface, the landslide width reached 80 m. Much closer to the crown, the width of the landslide was smaller. The landslide was 15 m thick on average, with a total volume of 160 000 m^3, and the main sliding direction was 320°.

The underlying bedrock of the Tangjiaxi slope is a Nantuo Formation (Z_n) and Guanyintian Formation of Sinian (Z_g) according to the drilling reconnaissance and field survey. The lithology is grey-green till conglomerate and red metamorphosed quartz sandstone. The dip of schistosity of the rock mass is 300–310° with the dip angle of 30–40°. Two groups of faults with high dip angle are developed under the slope, whose strike direction is nearly parallel to the valley. The fault belt is mainly mylonite (Fig. 5). Influenced by the fault, fissures are developed, and there are mainly two groups of the structure planes: (1) fissures with a dip of 20–30° and a dip angle of 60–70° and (2) fissures with a dip of 300–320° and a dip angle of 65–70°. Red or brown clay can be seen in some fissures. Two groups of structural planes and schistosity intersected mutually cataclasite structure rock mass were formed in the Tangjiaxi slope.

After the landslide failed, cataclasite structure rock mass disintegrated quickly. The accumulation of sliding mass was mainly composed of rock blocks of different sizes. Medium and large rock blocks were mainly in the lower-middle part, with a maximum length of rock blocks of about 2.5 m. Rock blocks in the accumulation, in a sharply angular shape with an average diameter of 30–40 cm, are overhanging stacked in the accumulation zone (Fig. 6). The few gravelly soils on the accumulation site were mainly distributed on the flanks of the landslide and at the front edge of accumulation fan. These soils were mainly derived from weathered layer and eluvial deposit of the original slope.

Part of the sliding mass was accumulated in the watercourse and some stayed on the slope. The landslide dam raised the river bed and halted part of the upstream water to form a small landslide lake. The landslide dam was high downstream and low upstream, with a bulge in the middle. Two terraces were formed on the vertical section. The dip angle of the deposits on the terrace was about 33°. The first slope terrace had an average elevation of about 180 m, 38 m long and 77 m wide, with a gradient of about 10°, while the second terrace had an average elevation of about 172.5 m, 75 m long and 98 m wide, with an average gradient of about 5–10°. The bulge was in the second terrace, with the top point of the elevation a.s.l. at about 175.5 m. The river was broken by the second terrace of the landslide, which can be seen in Fig. 7.

Witnesses reported that it took only several seconds for the landslide to slide into the water and form the landslide dam. Calculated at 10 s for the sliding duration time, the landslide barycenter is about 70 m above the still-water surface, and the sliding distance is about 120 m. It is roughly estimated that the biggest impact speed is about 24 m s^{-1} according to Newton's laws of motion. Huge impulse waves were triggered by the high-speed landslide. The impulse wave attacked the opposite bank, razed six houses to the ground, and cut trees to the root (Fig. 8a). Then, the impulse wave flowed both upstream and downstream. The high-speed wave destroyed all houses (Fig. 8b, d) and trees (Fig. 8c) within its path. Nine houses were destroyed in this tsunami event, eight houses were damaged, and 121 individuals of 17 families were affected. The impulse wave resulted in three deaths, nine people missing, and 11 people wounded, and six of them being badly hurt. Fortunately, the owners of five destroyed houses had gone out for work and had not stayed in the houses. Otherwise, the casualties would have been more severe.

Despite the 10 m depth of the watercourse in the landslide zone, the limited water gained a large amount of energy from the high-speed sliding and formed huge impulse waves. As shown in the field survey, the maximum run-up was 22.7 m and occurred in the opposite bank of the landslide; the upstream maximum run-up was 19.5 m and occurred in a gully about 100 m upstream. At the downstream, with the increase in distance from the source of impulse waves, the run-up decayed. The maximum run-up at the river mouth, where the Tangjiaxi stream flowed into the Chanxi stream, was 1.8 m (Fig. 8). As the Tangjiaxi stream flowed into the Chanxi stream nearly vertically, the water surface suddenly became very wide, the impulse waves decayed rapidly, and no sign of impulse waves was seen on either bank of the Chanxi stream.

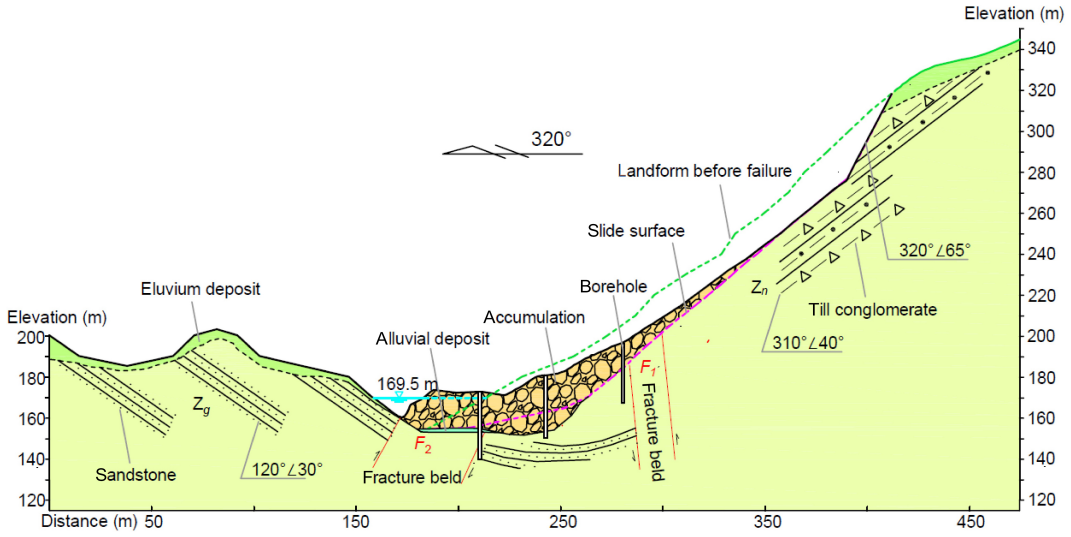

Figure 5. Geological engineering section of the Tangjiaxi landslide.

Figure 6. Accumulated blocks after the Tangjiaxi landslide failure, taken on 23 July 2014.

Figure 7. Profile photo of the Tangjiaxi landslide, taken on 23 July 2014, when the water level was 167 m a.s.l.

3.2 The granular flow coupling model

The computational domain which is considered to simulate the Tangjiaxi landslide-induced impulse wave by the full coupling numerical model covers the landforms of the valley where the Tangjiaxi landslide occurred. The domain is 792 m long and 684 m wide including the valley source of the Tangjiaxi stream at the tail of the Zhexi Reservoir, with the lowest elevation at 140.0 m and the maximum mountain elevation at 740.2 m (Fig. 9). The digital elevation model of the Tangjiaxi sliding mass is plotted based on the drilling survey and the topographic maps before and after the landslide, with a volume of about 158 000 m^3. As the Tangjiaxi landslide failed under the condition of persistent rainstorm, the gaps between grains were basically filled with rainwater. Thus, the sliding material can be assumed to be saturated. During the process of the Tangjiaxi landslide motion, there were two distinct phases for the motion of rocky grains: the start-up and moving phase and the impact–stop phase in sequence. Impact in the first phase mainly occurred among grains and then in the second phase mainly between leading grains and the opposite bank. Therefore, two elastic restitution coefficients were adopted, and 0 was taken in the second phase when the leading granular flow impacts the bank. After trial calculation, 0.2 was taken in the first phase when the impact mainly occurred among grains, which makes the simulation results more realistic. The parameters required for granular flow motion calculation are as shown in Table 1. The parameters of density, average diameter, and initial porosity of rock grains were determined through field survey and laboratory tests. The Tangjiaxi sliding mass was stationary initially and started moving under gravity. The granular flow moved and coupled with water after exposure to the river water.

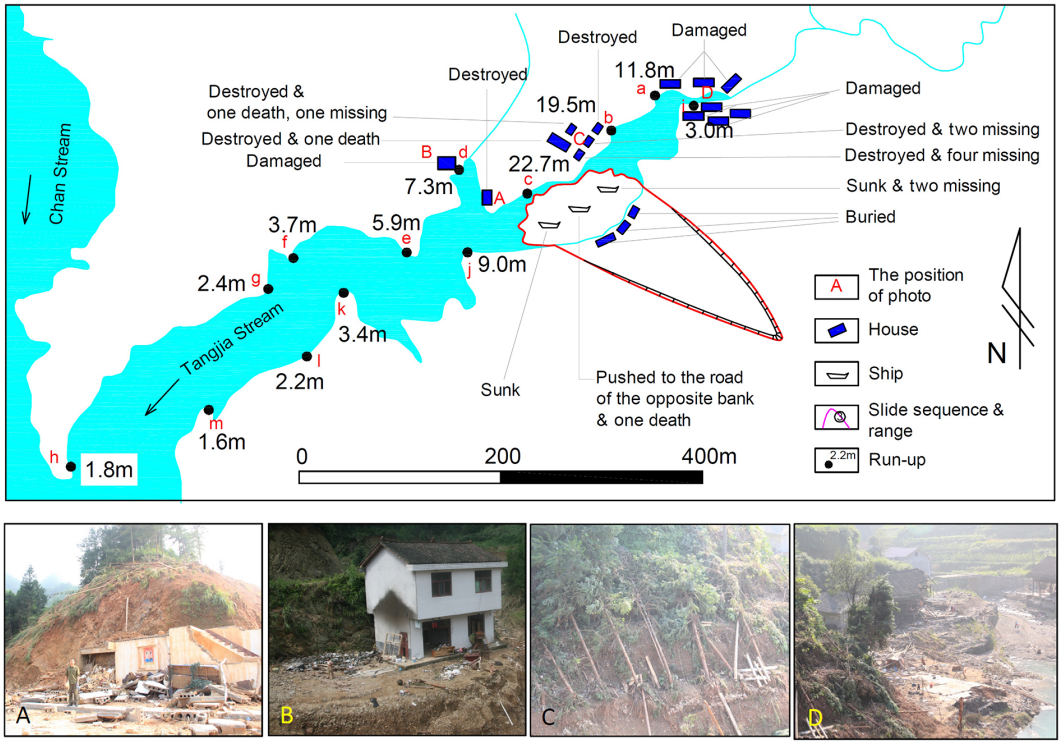

Figure 8. The plot of run-up of the impulse wave generated by the Tangjiaxi landslide. The photos describe the scenarios of houses and trees damaged where marked by **(a)**, **(b)**, **(c)**, and **(d)** in the upper map.

Table 1. Main parameters for Mih equation calculation.

Parameter	Value	Parameter	Value
Fluid density	1000 kg m^{-3}	Grain restitution coefficient	0.2/0
Fluid viscosity	0.001 pa s	Average grain diameter	0.4 m
Grain density	2640 kg m^{-3}	Global vent coefficient	0.001

The water surface elevation in the model is 169.5 m a.s.l., and the still-water surface is the initial condition. X_{min} surface is the zero flow boundary to ensure a constant water volume of the Tangjiaxi stream. Z_{max} (water surface) is zero pressure boundary or free surface. Z_{min} surface, X_{max} surface, Y_{min} surface, and Y_{max} surface are all solid wall surfaces which are far away from the valley, so they are also zero flow boundaries. With the finite volume method with Euler algorithm adopted, there are 13 001 472 units in total in a grid of 2 m × 2 m × 2 m. The simulation calculation of the numerical model lasts 30 s. After 6 s, the model comes into phase 2 as the leading granular flow impacts the bank based on trial calculations.

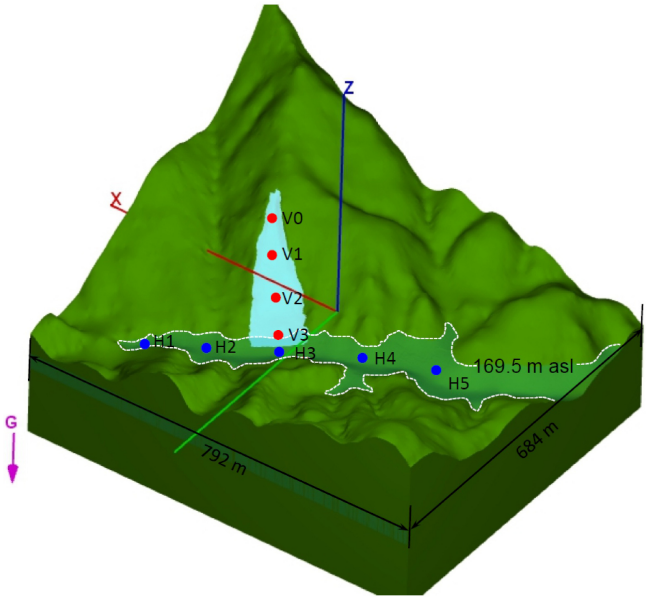

Figure 9. Numerical model for the Tangjiaxi landslide-induced impulse waves. The red points refer to the velocity monitoring points of the sliding mass motion, and the blue ones refer to the process monitoring points for water level.

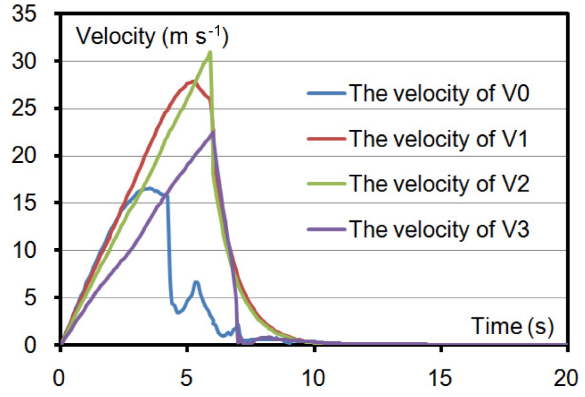

Figure 10. Depth-averaged velocity process plot of monitoring points in the sliding mass. See Fig. 9 for positions of VO–V1.

3.3 Numerical results

In this simulation, the following aspects of the Tangjiaxi landslide event are analyzed: the motion process of the sliding mass and the process of impulse wave and the model's validity, which was also checked through comparison with the field survey results.

Landslide movement process

The model analysis starts with the movement of the sliding mass. The depth-averaged velocity curves at different elevation points of the sliding mass show that the time to reach the maximum velocity varies for different parts of the landslide. Most of the landslide parts reached the maximum velocity before impacting the opposite valley at the sixth second. The maximum sliding velocity of the area at the rear edge (V0) was about 16.6 m s^{-1} and at the middle of the sliding slope (V2) about 30.9 m s^{-1}, which was possibly the maximum motion velocity of the sliding slope. The V3 point was located at the riverside with an elevation of 169.5 m, and V3's velocity was approximated to the speed at which the sliding mass impacted water, up to 22.5 m s^{-1} (Fig. 10). The value was equivalent to the maximum impact velocity estimated in field, which was 24 m s^{-1}. After the sliding mass impacted the opposite valley, the motion velocity of different parts of the sliding mass dropped sharply; when it reached 10 s, the value at the middle and lower parts of the sliding mass was generally lower than 1 m s^{-1}, and at the upper part it was lower than 3 m s^{-1}. After 19 s, the velocity of the sliding mass was lower than 1 m s^{-1} overall.

Observed from the landslide configuration at different times, the motion of the sliding granular flow on land is generally within the scope of the sliding mass. After $t = 4.0$ s, the sliding mass started to occupy the watercourse and extended to the upstream and the downstream, forming a fan shape (Fig. 11). It can be seen from the comparison with the final plane shape of the watercourse that numerical simulation results show a more ideal fan-shaped accumulation (Mohammed and Fritz, 2005) and that the landslide dam shape formed in the numerical simulation differed from the actual situation (Fig. 12). This was possibly attributed to the presumption in the numerical model – i.e., the solid gains are ideally spherical, with a similar grain size.

The depth profile of section A-A′ (Fig. 12) in Fig. 13 and the depth process of V0–V3 in Fig. 14 show that the solid grains of the sliding mass gradually moved toward the valley and accumulated (Yavari-Ramshe et al., 2015). At $t = 2.1$ s, substances in the sliding mass slid to the river bed. Substances with an elevation of over 200 m moved at high velocity, so sliding mass in the area started to thin. After 2.1 s,

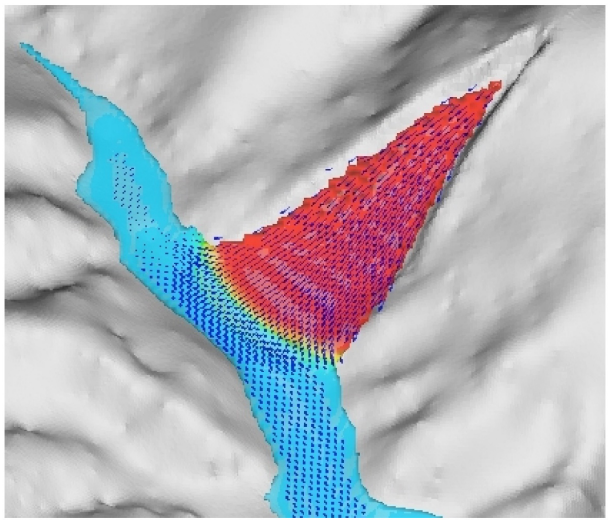

Figure 11. Instantaneous state of the Tangjiaxi landslide and river surface at $t = 4.0$ s. In the figure, the red area is the Tangjiaxi sliding mass, the cyan one is water, and the blue arrow is the motion direction of unit mass points.

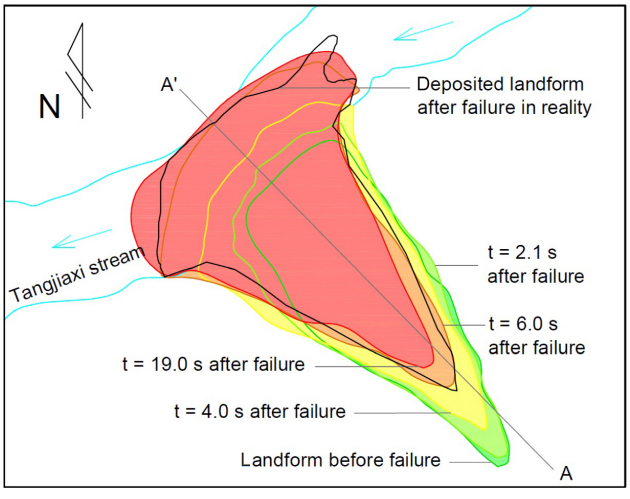

Figure 12. Changes of plane shape after the Tangjiaxi landslide failure.

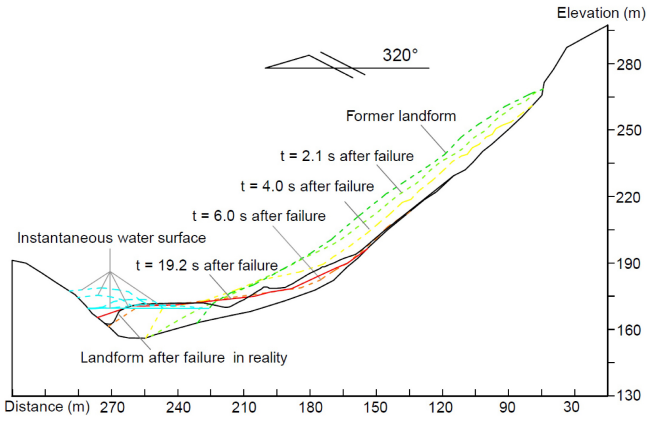

Figure 13. A-A′ section form after the Tangjiaxi landslide failure.

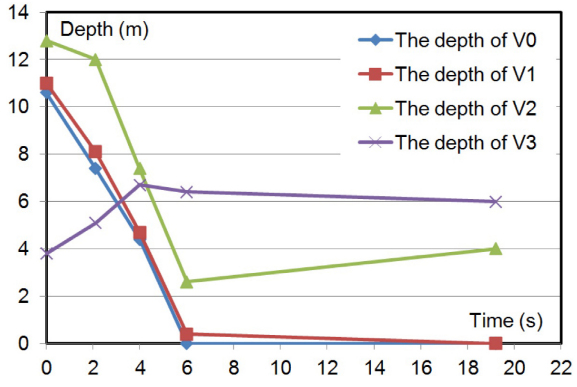

Figure 14. Depth process plot of monitoring points in the sliding mass.

the sliding mass started to occupy the river bed at a large scale. At $t = 4.0$ s, a small accumulated platform appeared in its early form in the valley and kept moving in the opposite direction. At $t = 6.0$ s, the slide front edge impacted the bank slope of the valley, when the landslide formed a large sliding dam in the valley and almost dammed the watercourse. At $t = 19.2$ s, the landslide configuration was similar to that at $t = 6.0$ s, and it remained unchanged, forming a landslide dam with an average elevation of about 171 m. The actual average elevation of the landslide dam formed was about 172.5 m. From the section landform after the landslide deposited, we can see that the actual landform after the landslide had an obvious two-step platform, while the simulated result was only a large one-step landslide platform, but their surface lines were similar.

Process of impulse waves

The motion results of the Tangjiaxi landslide simulated by the granular flow model show no significant differences from those seen in the field survey, basically reflecting the real motion process and characteristics of the landslide. A huge impulse wave was induced in the stream due to the motion of granular flow.

After the sliding mass occupied the watercourse, it pushed and supported the river water to move outwards and upwards in an arc shape (Fig. 13 and I in Fig. 15), similar to the forming of the impulse wave induced by the Qianjiangping landslide. At $t = 6.0$ s, an arc-shaped water wall formed on the river surface, which was about 10 m high and with a maximum water velocity of about 12.0 m s^{-1}, impacting the opposite bank and the upstream and downstream (II in Fig. 15). The residential area in area C was impacted first at the maximum impact velocity of 11.5 m s^{-1} (III in Fig. 15), resulting in a maximum run-up of 16.5 m in the area. At $t = 9.6$ s, water reached to the ridge near A, with a maximum traveling velocity of 12.1 m s^{-1} (IV in Fig. 15). At $t = 11.1$ s, water flowed over the ridge and impacted the houses of area A, with a maximum velocity of 11.6 m s^{-1}. At $t = 14.4$ s, impulse waves started to impact houses in B, with a maximum velocity of about 7.0 m s^{-1} (V in Fig. 15). After 16.3 s, impulse waves spreading upstream reached the residential area in D, with the maximum water flow impact velocity dropping to 3.8 m s^{-1} (VI in Fig. 15). Based on the numerical results, it took about 20 s for the impulse waves to move from the starting point in the landslide zone to the first residential area. The impulse waves attacked at high velocity and caused serious house damages and heavy casualties in the area.

As can be seen in Fig. 2, the Tangjiaxi valley is narrow. Therefore, it is hard to distinguish the generation, propagation, and run-up phases of the impulse wave. Accordingly, this event was not a typical landslide-induced impulse wave. As can be observed in the water level lines of various points in the Tangjiaxi river surface in Fig. 16, there was only one large peak for the impulse waves, close to the landslide impact area (H3 in Fig. 16). Since the upstream of the landslide was quickly dammed after the impulse waves arrived, water arriving upstream failed to flow smoothly and therefore formed a temporary upsurge upstream (Wang et al., 1986). The maximum upsurge in the upstream was up to 172.5 m (H2 in Fig. 16), and the upstream water level remained at about 171.6 m at 30 s. After a relatively large impulse wave, wave amplitude fluctuation in the landslide downstream watercourse attenuated (H4 in Fig. 16).

During the generation of this atypical landslide-induced impulse wave, it was hard to determine the maximum height of the first wave in the watercourse. The maximum propagating height of the wave in the peripheral watercourse of the landslide zone was about 8.0 m, located at the downstream of the landslide. The maximum run-up of the landslide was calculated to be 21.8 m at the opposite bank of the landslide; the run-up of this point in the field survey was 22.7 m. The slope at the opposite bank of the landslide was directly impacted by the impulse wave, with a relatively higher run-up. Overall, the run-up was higher in the area where the landslide slid into water and gradually decreased in the periphery with the increase in distance. Table 2 shows the run-up at the bank

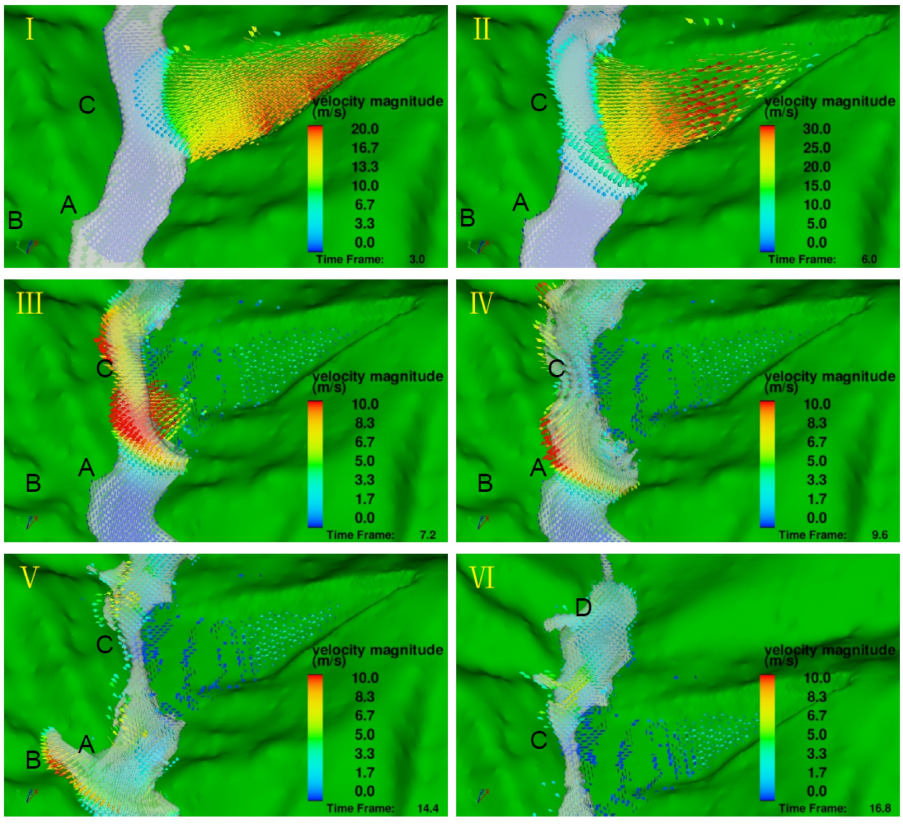

Figure 15. Transient condition of river water and the vector diagram of mass. The arrows indicate the direction of movement and the colors indicate the magnitudes shown in legend.

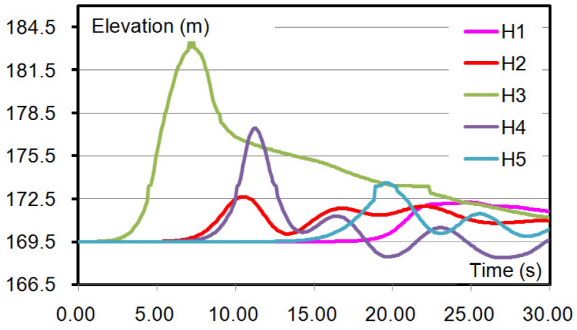

Figure 16. Hydro-process line of various points in watercourse. See Fig. 9 for locations of H1–H5.

surveyed in the field and the corresponding calculated values. The correlation coefficient (R^2) of these two sets of data was 0.98, with an average error of 11 %, indicating that calculated results adequately match with actual survey results, so the numerical model for landslide-induced impulse wave is reasonable and valid.

The equations of Baglad and Mih were obtained from the experiments of sphere grains, and there is non-coherence among the grains. Although some parameters are taken by back analysis in this case, the dynamic capacity of sphere grains is bigger than grains with other shape, which makes the energy transferred to water higher. Meanwhile, as rock mass begins to disintegrate in the actual situation as it slides into water, the coherence between rocks deserves consideration in the dynamic process. Therefore, the run-up values simulated are larger than investigations in general. Consideration of coherence and shape of grain is a main modification direction for this granular flow coupling model, which might improve its realism for a wider range of applications.

4 Conclusions

In this paper, a full coupling numerical model for landslide-induced impulse wave was developed. The non-coherent granular flow model of Mih (1999) was used to simulate the dynamic characteristics of the Tangjiaxi rockslide, and the two-phase flow model and RNG model were used to simulate the impulse waves while the granular flow impacted water.

The Tangjiaxi rocky granular flow slid into the watercourse and then moved to the upstream and the downstream, forming a fan shape, and depositing a landslide dam in the valley, damming the watercourse. The sliding mass impacted water at the maximum velocity of 22.5 m s^{-1} and at the mo-

Table 2. The calculated and measured run-up values at different points.

North run-up (m)	Position	g	f	e	d	c	b	a
	Investigation	2.4	3.7	5.9	7.3	22.7	19.5	11.8
	Calculation	3.3	3.6	6.5	7.0	21.8	17.3	12.1
South run-up (m)	Position	l	k	j	i			
	Investigation	2.2	3.4	9.0	3.0			
	Calculation	3.2	4.1	9.2	3.7			

ment the maximum celerity of the wave was 12.1 m s^{-1}. It was an atypical impulse wave at the point where the landslide slid into water, where the phases of generation, propagation, and run-up of the impulse wave were hard to distinguish. The impulse wave induced by the landslide directly attacked the opposite residential area, with a maximum run-up of 21.8 m as calculated. The landslide dam formed hindered the downward flowing of water upstream, causing a temporary upsurge.

The landslide dam configuration and impulse wave run-up calculated were well fit with the actual survey results. Therefore, the coupling model based on non-coherent Mih granular flow performed well in the whole-process analysis of the Tangjiaxi landslide-induced impulse wave. The framework of this coupling numerical model deserves more attention and further improvement.

Data availability. No data sets were used in this article.

Competing interests. The authors declare that they have no conflict of interest.

Acknowledgements. This work was supported by the National Natural Science Foundation of China (project ID: 41372321) and National Science and Technology Support (ID: 2012BAK10B01). Additionally, the authors would like to thank Xie from the Tangjiaxi village, who provided us with his photos and other useful information to us.

Edited by: K.-T. Chang
Reviewed by: two anonymous referees

References

Abadie, S., Morichon, D., Grilli, S., and Glockner, S.: Numerical simulation of waves generated by landslide using a multiple-fluid Navier-Stokes model, Coast. Eng., 57, 779–794, 2010.

Alvarez–Cedrón, C. and Drempetic, V.: Modeling of fast catastrophic landslides and impulse waves induced by them in fjords, lakes and reservoirs, Eng. Geol., 109, 124–134, 2009.

Ataie-Ashtiani, B. and Malek Mohammadi, S.: Near field amplitude of subaerial landslide generated waves in dam reservoirs, Dam. Engineering, 17, 197–222, 2007.

Ataie-Ashtiani, B. and Malek-Mohammadi, S.: Mapping impulsive waves due to subaerial landslides into a dam reservoir: a case study of Shafa-Roud Dam, Dam. Engin., 18, 1–25, 2008.

Ataie–Ashtiani, B. and Nik–Khah, A.: Impulsive waves caused by subaerial landslides, Environ. Fluid Mech., 8, 263–280, 2008.

Bagnold, R. A.: Experiments on a gravity-free dispersion of large solid spheres in a Newtonian fluid under shear, Proc. R. Soc. Lon. Ser. A, 225, 49–63, 1954.

Ball, J. W.: Hydraulic model studies, wave action generated by slides into Mica Reservoir, Technical report, Western Canada Hydraulic Laboratories, Vancouver, Canada, 1970.

Basu, D., Green, S., Das, K., Janetzke, R., and Stamatakos, J.: Numerical simulation of surface waves generated by a sub-aerial landslide at Lituya Bay, Alaska, Proceeding of OMAE 2009, 28th international conference on ocean, offshore and arctic engineering, 1–14, 2009.

Brennen, C. E.: Fundamentals of multiphase flow, Cambridge University Press, Cambridge, 2005.

Choi, B. H., Kim, D. C., Pelinovsky, E., and Woo, S. B.: Three-dimensional simulation of tsunami run – around conical island, Coast. Eng., 54, 618–629, 2007.

Cremonesi, M., Frangi, A., and Perego, U.: A Lagrangian finite element approach for the simulation of water-waves induced by landslides, Comput. Struct., 89, 1086–1093, 2011.

Crosta, G. B., Calvetti, F., Imposimato, S., Roddeman, D., Frattini, P., and Agliardi, F.: Granular Flow and Numerical Modelling of Landslides, Debrisfall Assessment in Mountain Catchments for Local End-users, Technique Report, 3–5, 2001.

Crosta, G. B., S., Imposimato, and D., Roddeman: Monitoring and modelling of rock slides and rock avalanches, Italian Journal of Engineering Geology and Environment, 6, 3–14, 2013.

Das, K., Janetzke, R., Basu, D., Green, S., and Stamatakos, J.: Numerical simulations of tsunami wave generation by submarine and aerial landslides using RANS and SPH models, Proceeding of OMAE 2009, 28th international conference on ocean, offshore and arctic engineering, 1–14, 2009.

Davidson, D. D. and Whalin, R. W.: Potential landslide-generated water waves, Libby Dam and Lake Koocanusa, Montana, Technical report, Waterways Experiment Station of US Army Corps of Engineers, Vicksburg, 1974.

Davies, D. R., Wilson, C. R., and Kramer, S. C.: Fluidity: a fully unstructured anisotropic adaptive mesh computational modeling framework for geodynamics, Geochem. Geophy. Geosy., 12, 309–311, doi:10.1029/2011GC003551, 2011.

Du, B.: Tangyanguang landslide of Zhexi Reservoir: The first large-scale landslide occurred at early stage of impoundment in China, Proceeding of the 2nd Symposium on Rock & Soil and Engineering of China, Beijing, 918–922, 1988 (in Chinese).

Fritz, H. M.: Initial phase of landslide generated impulse waves, Thesis for the PhD, Zürich University, 2002.

Fritz, H. M., Hager, W. H., and Minor, H. E.: Lituya Bay case: rockslide impact and wave run–up, Science of Tsunami Hazards, 19, 3–22, 2001.

Fumihiko, I., Yalciner, A. C., and Ozyurt, G.: Tsunami Modelling Manual, http://www.tsunami.civil.tohoku.ac.jp/hokusai3/J/projects/manual-ver-3.1.pdf (last access: 9 May 2017), 2006.

Gabl, R., Seibl, J., Gems, B., and Aufleger, M.: 3-D numerical approach to simulate the overtopping volume caused by an impulse wave comparable to avalanche impact in a reservoir, Nat. Hazards Earth Syst. Sci., 15, 2617–2630, doi:10.5194/nhess-15-2617-2015, 2015.

Glimsdal, S., L'Heureus, J. S., Harbitz, C. B., and Pedersen, G. K.: Modelling of the 1888 Landslide Tsunami, Trondheim, Norway, Proceeding the Second World Landslide Forum "Landslide Science and Practice", Springer, 5, 73–79, 2013.

Hanes, D. M. and Inman, D. L.: Observations of rapidly flowing granular-fluid mixture, J. Fluid Mech., 150, 357–380, 1985.

Harbitz, C. B., Glimsdal, S., Løvholt, F., Kveldsvik, V., Pedersen, G. K., and Jensen, A.: Rockslide tsunamis in complex fjords: from an unstable rock slope at Åkerneset to tsunami risk in western Norway, Coast. Eng., 88, 101–122, doi:10.1016/j.coastaleng.2014.02.003, 2014.

Heller, V.: Landslide generated impulse waves: prediction of near field characteristics, Thesis for the PhD Zürich University, Thesis for the PhD, Zürich University, 2007.

Heller, V., Hager, W. H., and Minor, H. E.: landslide generated impulse wawes in reservoirs: basics and computation, Technical report, VAW, ETH Zurich, 2009.

Hertz, H.: Uber die beruhrung fester elastischer Korper, J. Reine Angew. Math., 29, 156–171, 1882.

Huang, B., Wang, S., Yin, Y., L, G., and Chen, X.: Fluid-solid coupling kinetic analysis on impulsive wave generated by rockfall, Journal of Jilin University (Earth Science Edition), 43, 1936–1942, 2013.

Huang, B., Yin, Y., Wang, S., Chen, X., Liu, G., Jiang, Z., and Liu, J.: A physical similarity model of an impulsive wave generated by Gongjiafang landslide in Three Gorges Reservoir, China, Landslides, 11, 513–525, 2014.

Huang, B., Yin, Y., and Du, C.: Risk management study on impulse waves generated by Hongyanzi landslide in Three Gorges Reservoir of China on June 24, 2015, Landslide, 13, 603–616, doi:10.1007/s10346-016-0702-x, 2016.

Huang, B. L., Yin, Y. P., Liu, G. N., Wang, S. C., Chen, X. T., and Huo, Z. T.: Analysis of waves generated by Gongjiafang landslide in Wu Gorge, Three Gorges Reservoir, on November 23, 2008, Landslides, 9, 395–405, doi:10.1007/s10346-012-0331-y, 2012.

Huber, A. and Hager, W. H.: Forecasting impulse waves in reservoirs, Proceeding 19th Congres Des Grands Barrages, ICOLD, 31, 993–1005, 1997.

Iverson, R. M., Reid, M. E., and Lahusen, R. G.: Debris-flow mobilization from landslides, Ann. Rev. Earth Planet. Sci., 25, 85–138, 1997.

Johnson, K. L.: Contact mechanics, Cambridge University Press, Cambridge, 1985.

Kamphuis, J. W. and Bowering, R. J.: Impulse waves generated by landslides, Proceeding 12th Coastal Engineering Conference, Washington DC, New York, 1, 575–588, 1970.

Li, S. H., Tang, D. H., and Wang, J.: A two-scale contact model for collisions between blocks in CDEM, Sci. China, 9, 1596–1603, 2015.

Mih, W. C.: High concentration granular shear flow, J. Hydraul. Res., 37, 229–248, 1999.

Mohammed, F. and Fritz, H. M.: Experiments on Tsunamis Generated by 3D Granular Landslides, Submarine Mass Movements and Their Consequences, edited by: Mosher, D. C., Adv. Nat. Technol. Haz., 28, 705–720, 2005.

Morris, J. P., Rubin, M. B., Block, G. I., and Bonner, M. P.: Simulations of fracture and fragmentation of geologic materials using combined FEM/DEM analysis, Int. J. Impact. Eng., 33, 463–473, 2006.

Muller, D. and Schurter, M.: Impulse waves generated by an artificially induced rockfall in a Swiss lake, Procedings 25th IAHR Congress, 4, 209–216, 1993.

Munjiza, A.: The Combined Finite-Discrete Element Method, Chichester, Wiley, 2004.

Pudasaini, S. P.: Some exact solutions for debris and avalanche flows, Phys. Fluids, 23, 043301, doi:10.1063/1.3570532, 2011.

Randall, J. L.: CLAWPACK Version 4.3 User's Guide, University of Washington, http://depts.washington.edu/clawpack/clawpack-4.3/doc/claw42/clawuser.pdf (9 May 2017), 2006.

Ren, K. J., Jin, F., and Xu, Q. Q.: Vertical Two-Dimensional Numerical Simulation for Landslide-Generated Waves, Journal of Yangtze River Scientific Research Institute, 23, 1–4, 2006 (in Chinese).

Sassa, K., Dang, K., Yanagisawa, H., and He, B.: A new landslide-induced tsunami simulation model and its application to the 1792 Unzen-Mayuyama landslide-and-tsunami distaster, Landslides, doi:10.1007/s10346-016-0691-9, 2016.

Savage, S. B.: Experiments of shear flows of cohesionless granular materials, Proceeding US – Japan Seminar on Continuum Mech and Stat Approaches in mechanics of granular materials, edited by: Cowin, S. C. and Satake, M., Gakujutsu Bunken Fukykai, Tokyo, Japan, 241–254, 1978.

Scheffers, A. and Kelletat, D.: Sedimentologic and geomorphologic tsunami imprints worldwide – a review, Earth. Sci. Rev., 63, 83–92, doi:10.1016/S0012-8252(03)00018-7, 2003.

Serrano-Pacheco, A., Murillo, J., and García-Navarro, P.: A finite volume method for the simulation of the waves generated by landslides, J. Hydrol., 373, 273–289, 2009.

Shakeri, M. M. and Sanders, B. F.: The LHLLC scheme for two-layer and two-phase transcritical flows over a mobile bed with avalanching, wetting and drying, Adv. Water Resour., 67, 16–31, 2014.

Silvia, B. and Marco, P.: Shallow water numerical model of the wave generated by the Vajont landslide, Environ. Model Softw., 26, 406–418, 2011.

Smilauer, E. C. V., Chareyre, B., Dorofeenko, S., Duriez, J., Gladky, A., Kozicki, J., Modenese, C., Scholtes, L., Sibille, L., Stransky, J., and Thoeni, K.: Yade Documentation, http://yade-dem.org/doc/index-toctree.html (last access: 9 May 2017), 2010.

Tappin, D. R., Watts, P., and Grilli, S. T.: The Papua New Guinea tsunami of July 17, 1998: anatomy of a catastrophic event, Nat. Hazards Earth Syst. Sci., 8, 243–266, doi:10.5194/nhess-8-243-2008, 2008.

Thomas, G.: Landslide occurrence as a response to land use change: a review of evidence from New Zealand, Catena, 51, 297–314, 2003.

Titov, V. V. and Gonzalez, F. I.: Implementation and Testing of the Method of Splitting Tsunami (MOST) Model, NOAA Technical Memorandum ERL PMEL-112, 1997.

Ursell, F., Dean, R. G., and Yu, Y. S.: Forced small amplitude water waves: a comparison of theory and experiment, J. Fluid Mech., 7, 3–52, 1960.

Utili, S. and Crosta, G. B.: Modeling the evolution of natural cliffs subject to weathering: 2. Discrete element approach, J. Geophys. Res.-Earth Surf., 116, F01017, doi:10.1029/2009JF001559, 2011.

Utili, S., Zhao, T., and Houlsby, G. T.: 3D DEM investigation of granular column collapse: evaluation of debris motion and its destructive power, Eng. Geol., 186, 3–16, 2014.

Walder, J. S., Watts, P., Sorensen, O. E., and Janssen, K.: Tsunamis generated by subaerial mass flows, J. Geophys. Res., 18, 2236–2255, 2003.

Wang, D. and Campbell, C.: Reynolds analogy for a shearing granular material, J. Fluid Mech., 244, 527–546, 1992.

Wang, D. Y. and Liu, S. K.: Xintan landslide impulsive wave survey in June of 1985, Yangtze River, 10, 24–27, 1986.

Wang, F.-W., Zhang, Y.-M., Huo, Z.-T., and Tatsunori Matsumoto, B.-L. H.: The July 14, 2003, Qianjiangping landslide, Three Gorges Reservoir, China, Landslides, 1, 157–162, 2004.

Watts, P., Grilli, S. T., Kirby, J. T., Fryer, G. J., and Tappin, D. R.: Landslide tsunami case studies using a Boussinesq model and a fully nonlinear tsunami generation model, Nat. Hazards Earth Syst. Sci., 3, 391–402, doi:10.5194/nhess-3-391-2003, 2003.

Wieland, M., Gray, J. M., and Hutter, K.: Channelized free-surface flow of cohesionless granular avalanches in a chute with shallow lateral curvature, J. Fluid Mech., 392, 73–100, 1999.

Xing, A., Xu, Q., Zhu, Y., Zhu, J., and Liang, Y.: The August 27, 2014, rock avalanche and related impulse water waves in Fuquan, Guizhou, China, Landslides, 13, 411–422, 2016.

Yakhot, V. and Orszag, S. A.: Orszag, Renormalization group analysis of turbulence, I. basic theory, J. Sci. Comput., 1, 3–51, 1986.

Yakhot, V. and Smith, L. M.: The renormalization group, the e-expansion and derivation of turbulence models, J. Sci. Comput., 7, 35–61, 1992.

Yavari-Ramshe, S., Ataie-Ashtiani, B., and Sanders, B. F.: A robust finite volume model to simulate granular flows, Comput. Geotech., 66, 96–112, 2015.

Yavari-Ramshe, S. and Ataie-Ashtiani, B.: Numerical modeling of subaerial and submarine landslide-generated tsunami waves–recent advances and future challenges, Landslides, 13, 1325–1368, doi:10.1007/s10346-016-0734-2, 2016.

Yin, K. L., Du, J., and Wang, Y.: Analysis of surge triggered by Dayantang landslide in Shuibuya Reservoir of Qingjiang River, Chin. J. Rock Soil Mech., 29, 3266–3270, 2008.

Yin, Y., Huang, B., Chen, X., Liu, G., and Wang, S.: Numerical analysis on wave generated by the Qianjiangping landslide in Three Gorges Reservoir, China, Landslides, 12, 355–364, 2015a.

Yin, Y., Huang, B., Liu, G., and Wang, S.: Potential risk analysis on a Jianchuandong dangerous rockmass-generated impulse wave in the Three Gorges Reservoir, China, Environ. Earth Sci., 74, 2595–2607, 2015b.

Yin, Y., Huang, B., Wang, S., and Li, J.: Potential for a Ganhaizi landslide-generated surge in Xiluodu Reservoir, Jinsha River, China, Environ. Earth Sci., 73, 3187–3196, 2015c.

Zhang, D. and Whiten, W. J.: The calculation of contact forces between particles using spring and damping models, Powder Technol., 88, 59–64, 1996.

Zhao, T., Utili, S., and Crosta, G. B.: Rockslide and impulse wave modelling in the Vajont Reservoir by DEM-CFD Analyses, Rock Mech. Rock Eng., 49, 2437–2456, doi:10.1007/s00603-015-0731-0, 2015.